Environmental Technology & Innovation 28 (2022) 102947

Contents lists available at ScienceDirect

Environmental Technology & Innovation

journal homepage: www.elsevier.com/locate/eti

UV-light-induced photocatalytic response of Pechini sol–gel synthesized erbium vanadate nanostructures toward degradation of colored pollutants

Atefeh Karami [a], Rozita Monsef [a], Mustafa Ridha Shihan [b], Laith Yassen Qassem [c], Mayadah W. Falah [d], Masoud Salavati-Niasari [a,*]

[a] Institute of Nano Science and Nano Technology, University of Kashan, Kashan, P. O. Box. 87317-51167, I. R., Iran
[b] College of Pharmacy, Ahl Al Bayt University, Kerbala, Iraq
[c] Department of Medical Laboratory Technics, AlNoor University College, Bartella, Iraq
[d] Building and Construction Engineering Technology Department, AL-Mustaqbal University College, Hillah 51001, Iraq

ARTICLE INFO

Article history:
Received 15 July 2022
Received in revised form 16 October 2022
Accepted 18 October 2022
Available online 25 October 2022

Keywords:
Erbium vanadate
Nanostructures
Photocatalyst
Modified Pechini
Electron microscopy

ABSTRACT

This study investigates synthesis of erbium vanadate nanostructures *via* carboxylic-assisted pechini method to optimization the morphology, size and physicochemical properties. The optimized $ErVO_4$ nanoparticles with range size of 12–98 nm were subjected to photocatalytic ability for dye decolorization of Methyl orange (MO), Erythrosine (ER), and Methylene blue (MB) using ultraviolet irradiation. The correlation between the operational parameters (pollutant concentration and catalyst loading) and optoelectronic properties in addition to the catalytic performance of the $ErVO_4$ structure is reported. The ideal condition for activity of $ErVO_4$ nano-photocatalyst achieved in the 10 ppm aqueous solution of MB with catalyst loading of 0.05 g which presents 77.85% efficiency for decolorization of colored pollutant model. The recycle photocatalytic efficiency after 4 cycles is about 69.25%. Additionally, the photocatalytic mechanism direction studied in the presence of some scavengers which confirms the role of hydroxyl radical in the removal of MB. The magnetic properties of $ErVO_4$ studied through VSM which shows the paramagnetic behavior with saturation magnetization is 1.3341 emu g^{-1}.

1. Introduction

The category of materials based on vanadium oxide has concerned superior consideration owing to their unique physical, optical, and magnetic features. It is recognized that composition stoichiometry in vanadium oxide-based materials can convert into diverse complex vanadates, namely metavanadate, pyro-vanadate and orthovanadate.

These features are correlated to the vanadium electronic configuration. This element is frequently found in oxides in all the oxidation states that can be between +5 to −3 in an aqueous solution (Aljeboree et al., 2021; Zhang et al., 1998; Alshamusi et al., 2021). Rare earth vanadate (RVO_4) has special attention for searching their fascinating relationships among the crystal construction, electronic/atomic structure, and varied requests such as rare earth element free white light-emitting devices, supercapacitors, photocatalysis and colored pollutant discoloration, electrode materials for solid-state batteries, and drug recognition (Abdulsahib et al., 2021; Hunge et al., 2021; Ji et al., 2017; Zonarsaghar et al., 2022;

* Corresponding author.
E-mail address: salavati@kashanu.ac.ir (M. Salavati-Niasari).

https://doi.org/10.1016/j.eti.2022.102947

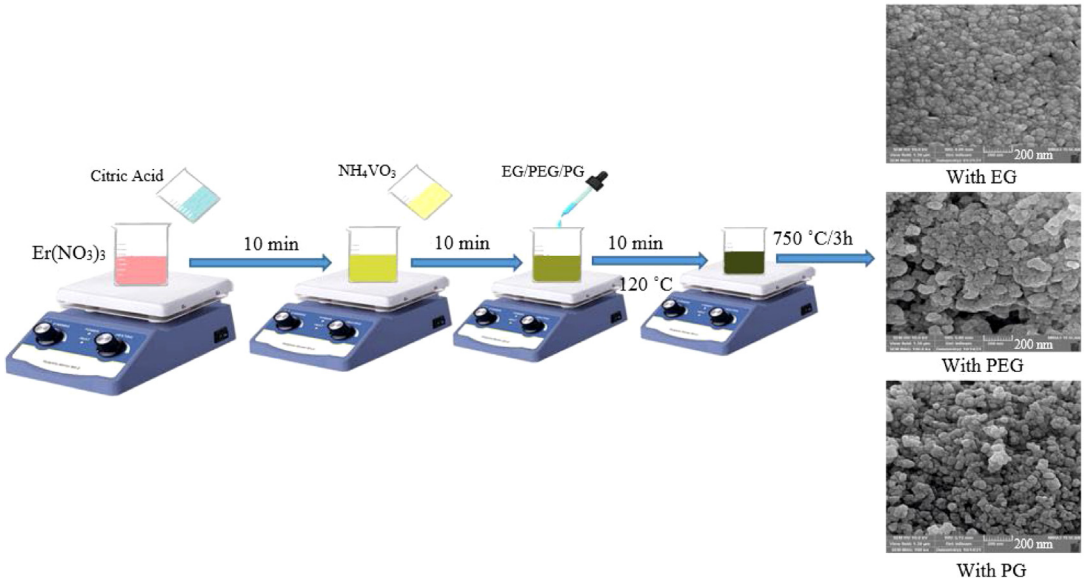

Scheme 1. Schematic illustration for step-by-step synthesis of $ErVO_4$ nanostructures with Pechini method.

Aljeboree et al., 2020). Today, vanadium oxide-based materials are mostly synthesized at lower calcination temperatures compared with conventional ceramic materials, which is consistent with the necessity of low energy consumption for material production (Ghiyasiyan-Arani and Masjedi-Arani, 2016; Ghiyasiyan-Arani et al., 2016a; Mahdi et al., 2022).

$ErVO_4$ is one of the rare earth vanadate compounds with layered crystal structures. Rare earth vanadate materials with diverse shapes and morphologies have been manufactured. Some authors observed that $ErVO_4$ has photo-absorption in the range of UV–visible light, and the band gap value was 3.24 eV. The obtained optical band gap shows that the $ErVO_4$ structures are more possible to illustrate a semiconducting action that is crucial for the Ultra violet induced photocatalytic decolorization of colored contaminants (Abedini, 2017; Obregón et al., 2018). The synthesis procedure has an important effect on the material characteristics; it can control the features and usage of these compounds. The greatest kinds of oxide materials are still manufactured by the conventional synthesis way such as solid-state or mechanical methods which consume high energy, but moderately high temperatures are essential in this synthesis mechanism due to the limited diffusion through the sintering or calcination process (Grabowska, 2016; Kim et al., 2018; Jasim et al., 2022).

Owing to the drawbacks of mechanical methods with high energy, chemical ways have emerged to manufacture oxide compounds including solvothermal, precipitation, sonochemical, sol–gel and etc. (Ghiyasiyan-Arani et al., 2016b; Ganduh et al., 2021a,b). Also, some biosynthesis methods suggest for preparation of metal oxide materials using plant extract, vegetable waste, flower extract, algae, fungus and bacteria (AlNadhari et al., 2021; Ameen et al., 2021, 2019; Moghadam et al., 2022; Mythili et al., 2018; Saravanan et al., 2018; Mahdi et al., 2020, 2021).

The modified sol–gel (Pechini process) can be considered by the esterification reaction in the presence of carboxylic acids and the creation of a polymeric system followed by the thermal treatment, crystals can be attained. The pechini method has some advantages consisting of production materials with low-cost, suitable size and morphology control, uniform structures, and ideal phase purity at low calcination temperature (Mamonova et al., 2017; Souza et al., 2021) (see Scheme 1).

Size reduction of materials to nanometric scale generally presents innovative attributes compared to bulk or micrometric materials. These phenomena basically ascend from the limited size and surface defects of material and because its electronic attributes start to alteration owing to the quantum size effect (Fernandez-Garcia et al., 2004). Consequently, the capability to scientifically manipulate nanostructures is a significant task in current materials knowledge (Fadillah et al., 2022; Wang et al., 2014). Highly effective and reusable catalyst is always desirable for practical photocatalytic applications (Li et al., 2020). The semiconductor-based photocatalysts can provide a novel insight into designing light-driven photocatalyst with excellent photocatalytic performance (Liu et al., 2022; Yang et al., 2020). Different Nobel metal or metal oxide materials used for degradation of colored or colorless pollutants such as methylene blue, methyl orange, Congo red, 4-nitrophenol, 2,4-dinitrophenylhydrazine, potassium hexacyanoferrate (Ahmad et al., 2019; Jaleh et al., 2020; Musadiq Anis et al., 2022; Nasri et al., 2021)

This research presents an optimized synthesis of $ErVO_4$ nanostructures by the pechini method and comparative study of carboxylic and diol effect of the morphology and size of obtained products. The effect of the synthesis condition can change the particles morphology, size, crystalline structure, and optical properties. So, the activity of synthesized $ErVO_4$ on the decolorization of colored pollutants was studied on the ER, MO and MB as models with changing the operational

Table 1
Summarized synthesis condition and derived data from XRD and FE-SEM analysis.

Sample No.	Carboxylic acid	Diol	Crystallite size (XRD)/nm	Particle size range (SEM)/nm	Morphology
P1	Citric acid	EG	18.89	12–98	Uniform nanoparticle
P2	Malonic acid	EG	36.10	15–1036	Bulk structure
P3	Citric acid	PG	26.28	62–374	Agglomerated structure
P4	Citric acid	PEG	25.78	22–165	Non-uniform particles

parameters of catalyst loading and pollutant concentration. Also, the stability, cycle ability and mechanism process of obtained $ErVO_4$ nano-photocatalyst was investigated in the series of experimental test.

2. Material and method

The starting materials employed in the pechini sol–gel synthesis method of $ErVO_4$ samples including, $Er(NO_3)_3.6H_2O$ and NH_4VO_3, citric acid, malonic acid, ethylene glycol, propylene glycol and poly ethylene glycol, were acquired from a company of Aldrich and used as arrived without additional purification.

In order to synthesis of $ErVO_4$, 0.15 g $Er(NO_3)_3.6H_2O$ (0.33 mmol) and 0.35 g citric acid (1.82 mmol) were dissolved in deionized water. Next, the 0.039 g NH_4VO_3 (0.33 mmol) were dissolves at 70 °C in 20 ml deionized water and added to the above solution. The diol agent of ethylene glycol (2 drops) added to the resultant mixture and heated on the stirrer at 120 °C to formation of gel condition. The resultant gel dried in an oven for 24 h at 60 °C. The dried gel was treated in furnace at 750 °C for 3 h to further crystallization and remove the organic compounds of samples. The synthesis condition for preparation of ErVO4 summarized in Table 1 in terms of changing carboxylic acid and diol agent.

The obtained products were characterized by diverse methods and equipment. XRD diffractograms were recorded by an X-ray diffractometer device using Ni-filtered Cu Ka radiation (Philips-X'pertpro). FT-IR spectra were managed on Nicolet Magna- 550 spectrometer in KBr pellets. SEM micrographs were achieved on LEO-1455VP equipped with an energy dispersive X-ray spectroscopy. The EDS analysis with 20 kV hasten voltage was operated. TEM images were captured on a Philips EM208 transmission electron microscope with an accelerating voltage of 200 kV. The BET analysis was conducted at −196 °C using an automated gas adsorption analyzer (Tristar 3000, Micromeritics). The distribution of pore size was measured applying the desorption branch of the isotherm by the BJH way. Magnetic properties were measured using a vibrating sample magnetometer (VSM, Meghnatis Kavir Kashan Co., Kashan, Iran).

The photocatalytic response of provided $ErVO_4$ toward degradation of colored pollutants of erythrosine (ER), methyl orange (MO) and methylene blue (MB) were performed in 120 min under UV light. The specific ErVO4 dosage dispersed in 50 ml dye solution in a quartz vessel, aerated and took place for 30 min. Sampling was achieved at definite period by means of the UV–Vis spectrometer for absorbance evaluation.

3. Results

3.1. Chemical and crystallite structures (XRD, FT-IR, EDS)

Resultant samples synthesized in the different conditions (mentioned in Table 1) were analyzed via the XRD technique in the range of 10–80 degrees. The obtained phase for samples P1 (Fig. 1a), P2 (Fig. 1b), P3 (Fig. 1c), and P4 (Fig. 1d) is tetragonal $ErVO_4$ with space group of *I41/amd* well matched with reference pattern with code of 01-086-2349. The calculated crystallite size with the Scherrer equation for samples P1, P2, P3 and P4 are 18.89, 36.10, 26.28 and 25.78 nm respectively.

The chemical bands for $ErVO_4$ structures were studied using the FT-IR method. The display bands in Fig. 2 confirm the stretching and bending vibration of the hydroxyl category were situated at 3438 cm^{-1} and 1642 cm^{-1}. A band at 805 cm^{-1} is due to the coupling vibration between V=O and V–O–V, while the one at 448 cm^{-1} is assigned to V–O–V bending vibration. The elemental composition for the resultant sample of $ErVO_4$ was studied by the EDS technique and shows the presentment of Er, V, and O in the nanostructured sample (Fig. 3). Fig. 3 (a–d) presents the elemental composition of samples P1, P2, P3, and P4 respectively.

3.2. Microscopic structure and surface area (FE-SEM, TEM, BET)

According to the obtained FE-SEM images in Fig. 4 (a, b), effect of citric acid and malonic acid on the morphology of synthesized samples was investigated. The citric acid-assisted synthesized $ErVO_4$ (P1-Fig. 4a) has uniform particles in a range size of 12-−98 nm. However, the bulk $ErVO_4$ (P2-Fig. 4b) was achieved in the presence of malonic acid with a range size of 15-−1036 nm. The obtained results authenticate that citric acid is the optimum fuel for the synthesis of $ErVO_4$ on a nanoscale with uniform distribution. On the other hand, the effect of diol on the shape of samples was compared through FE-SEM images in Fig. 4(c, d). Sample P1, P3 and P4 were synthesized by EG (Fig. 4a), PG (Fig. 4c) and PEG (Fig. 4d)

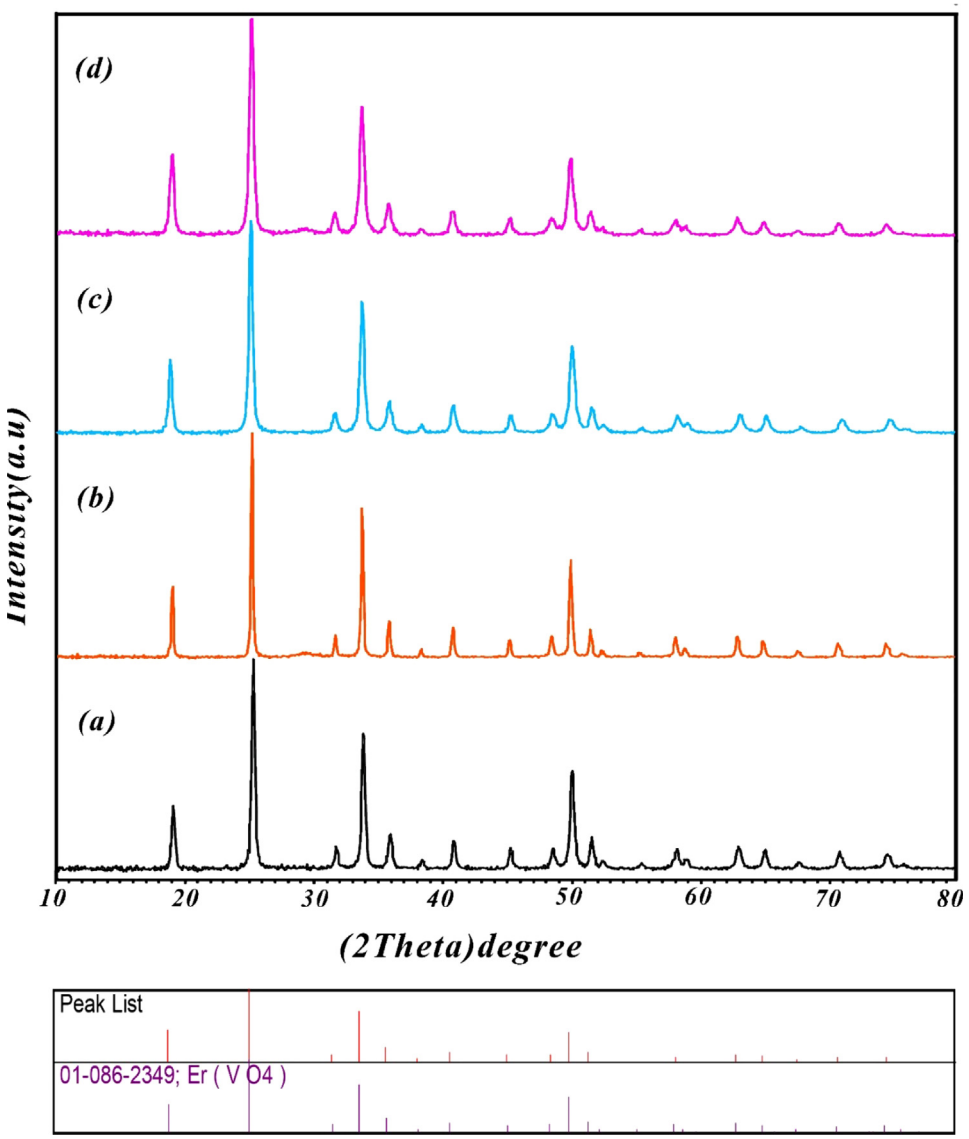

Fig. 1. Phase detection of synthesized $EuVO_4$ samples using XRD pattern. (a) P1, (b) P2, (c) P3, and (d) P4.

respectively. According to Fig. 4c, the resultant $ErVO_4$ has agglomerated structures in the range size of 62-−374 nm. The provided $ErVO_4$ in the presence of PEG (P4) shows particle size in the range of 22-−165 nm. So, the ideal $ErVO_4$ in these series of synthesis conditions is sample P1 which is prepared in the presence of citric acid and EG. The size distribution histogram for all samples displays in Fig. 5(a–d).

The mechanism for pechini synthesis of $ErVO_4$ was proposed in terms of the presence of carboxylic acid and diol. The carboxylic acid with the role of fuel and reductant, and metal ions with the role of oxidant can provide an oxidation–reduction reaction. Malonic acid as bidentate acid may coordinate with other malonic acids and associated in the reaction and does not chelate with metal ions due to bending configuration to form a ring structure. Therefore, the synthesized sample in the presence of malonic acid has a large size. Tridentate citric acid can react with glycols (hydroxyl groups) and stabilize by the polymerizing and chelating procedure, then the creation of large polymeric construction in the reaction medium. Citric acid formed complex structures with metal ions to prevent agglomeration of particles due to the hindrance effect of citric acid and prevent the growth of crystal facets. This mechanism can limit the crystal growth to obtain uniform nanoparticles.

The morphology of optimized sample (P1) of $ErVO_4$ which synthesized in the presence of citric acid and EG was further studied using TEM images (Fig. 6).

Thereinafter, the surface characterization of optimized sample (P1) was performed using BET-BJH methods. According to Fig. 7a, the resultant isotherm is the type IV with a H4 hysteresis loop (Leofanti et al., 1998). The pore size distribution

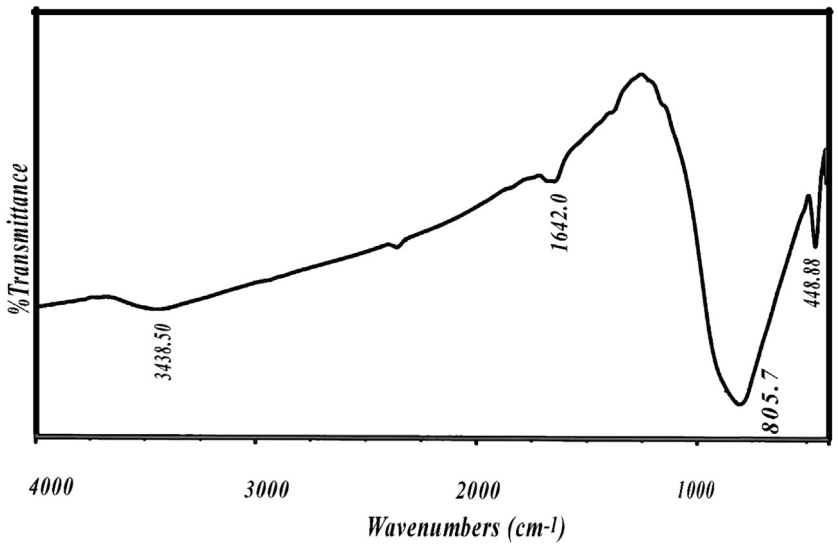

Fig. 2. Chemical band detection for synthesized $ErVO_4$ (P1) using FT-IR spectrum.

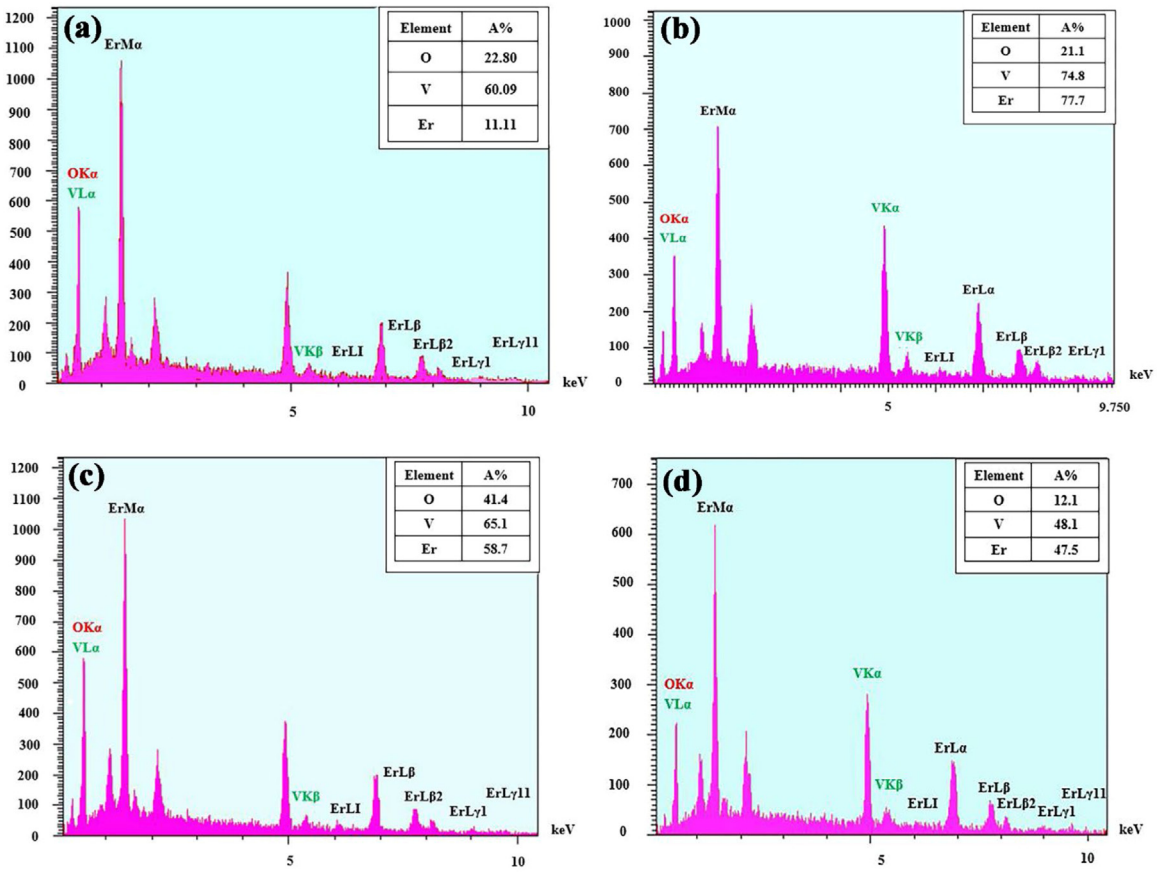

Fig. 3. Elemental detection of synthesized $ErVO_4$ samples. (a) P1, (b) P2, (c) P3 and (d) P4.

displays in Fig. 7b. The surface area and average pore size for this sample calculated about 16.919 m^2g^{-1} and 39.77 nm correspondingly. Total pore volume in $P/P_0 = 0.981$ reports as 0.1682 cm $^3g^{-1}$. The attained data shows the possibility of the $ErVO_4$ nanoparticles for catalytic application due to normal surface area and porosity.

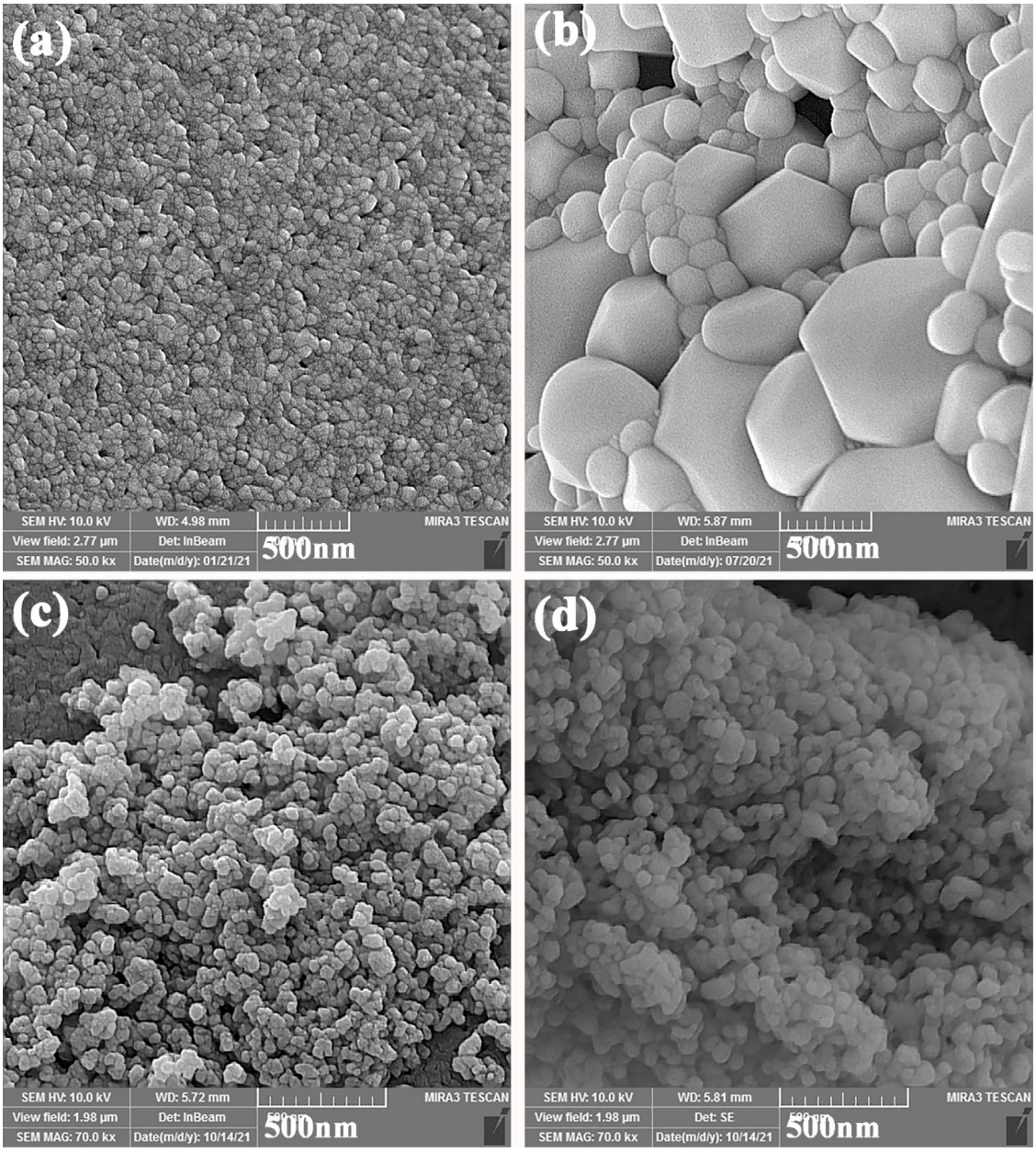

Fig. 4. Morphological investigation of synthesized $ErVO_4$ samples (a) P1, (b) P2, (c) P3 and (d) P4 using FE-SEM images.

3.3. Magnetic properties (VSM)

The room temperature hysteresis loops of $ErVO_4$ nanoparticles (P1) were restrained using VSM technique in the magnetic field range of −15,000 to 15,000 Oe that demonstrated in Fig. 8. Magnetic action of sample P1 was reflected paramagnetic material. The magnetic factors of saturation magnetization is 1.3341 emu g^{-1}. In order to the detected results, the provided sample is potential recyclable catalyst for applying in the water treatment usage.

3.4. Band gap (DRS)

The band gap is a significant information for check of the right kind of illumination source required for the photo-catalytic action. The UV-DRS analysis for sample P1 was conducted to estimation of optical properties and band gap of synthesized $ErVO_4$ which illustrates in Fig. 9a, b. The Tauk model for pure $ErVO_4$ was appraised by extrapolating $(KMh\upsilon)^n$

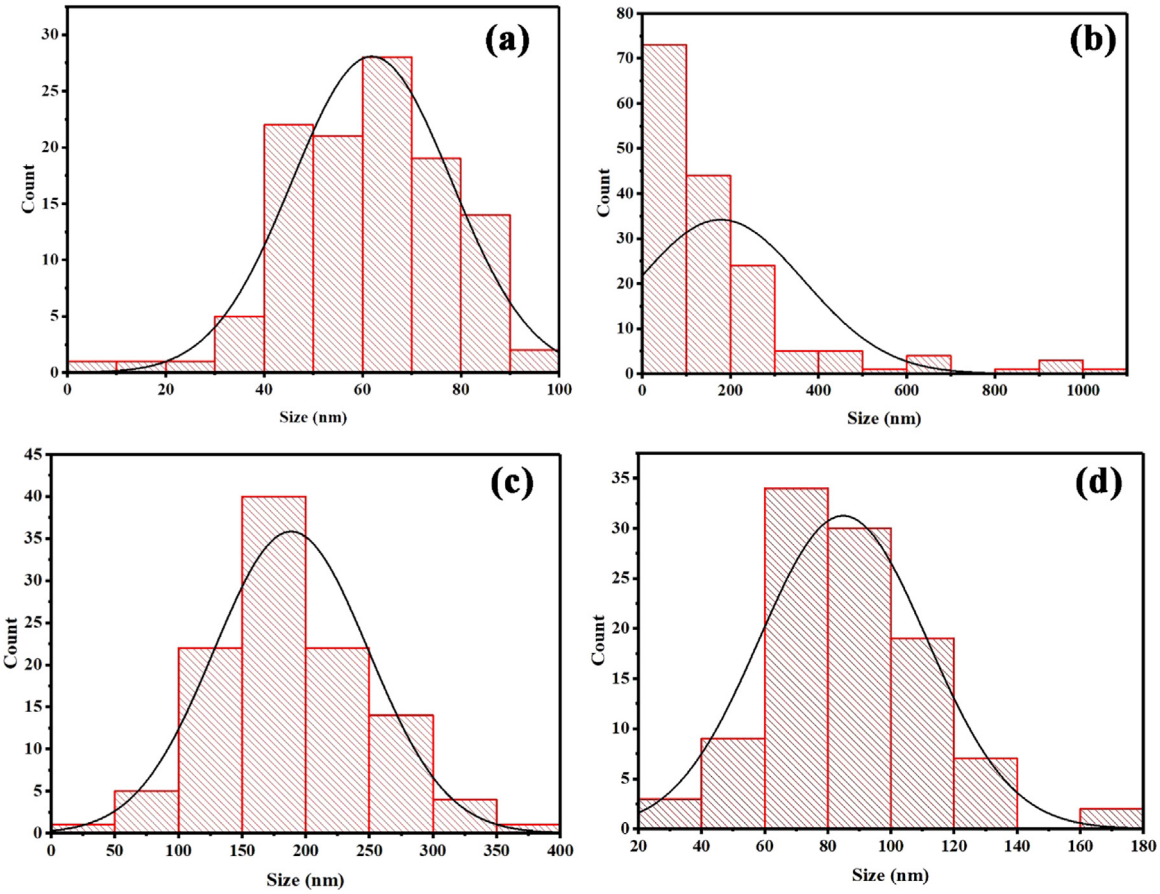

Fig. 5. Histogram for synthesized $ErVO_4$ samples (a) P1, (b) P2, (c) P3 and (c) P4 (count *vs.* size distribution).

curve versus hυ to zero. The correlated curve is displayed in Fig. 9. The assessed value for band gap is approximately 3.45 eV. So, the suitable illumination source is ultraviolet lamp due to the placement of wavelength in the range of 100-−400 nm (UV range).

3.5. Photocatalytic studies

In order to investigate the catalytic ability of synthesized $ErVO_4$ in optimized condition (P1) for removing the organic dye in an aqueous environment, a series of photocatalytic experiments were designed in terms of type of dye, dye concentration and catalyst loading. The first photocatalytic experiment was conducted to study the effect of type of dye. The erythrosine (ER), methyl orange (MO) and methylene blue (MB) were selected as colored pollutant models. The removal percentage versus time was recorded in Fig. 10a for comparing the type of colored pollutant. The removal percentage for MB (77.85%) is higher than MO (73.72%) and ER (70.94%) which specified the higher activity of $ErVO_4$ photocatalyst in cationic dyes than in anionic dyes. During the photocatalytic process of $ErVO_4$, the dye adsorption molecules on $ErVO_4$ is preferable for positively charged dyes (cationic) than for negatively charged dyes (anionic). This circumstance can be clarified in relation to the surface structure of $ErVO_4$ nanoparticles. On the surface of $ErVO_4$ nanoparticles, oxygen atoms with a high electron density are present. Thus, $ErVO_4$ has a negative charge and therefore adsorbs the cationic molecules (Ghiyasiyan-Arani and Masjedi-Arani, 2016).

The second photocatalytic experiment was performed to study the effect of dye concentration with 10, 15 and 20 ppm of methylene blue. According to Fig. 10b, the removal percentage in 10 ppm of MB is 77.85% and higher than the conducted experiments in 15 (65.98%) and 20 (53.11%) ppm concentrations. In high concentrations, a larger amount of pollutant molecules would saturate the binding sites found on the surface of the catalyst. It is clear that the decolorization performance reduced as the initial dye concentrations increased (de Luna et al., 2013).

The third experiment was studied to optimization of catalyst loading. The amount of 0.03, 0.05 and 0.07 g of $ErVO_4$ were used in 10 ppm methylene blue. The catalyst loading experiment is shown in Fig. 10c which explained the higher activity of $ErVO_4$ as a photocatalyst with the dosage of 0.05 g. The dye removal for this experiment exhibits 52.65%, 77.85%

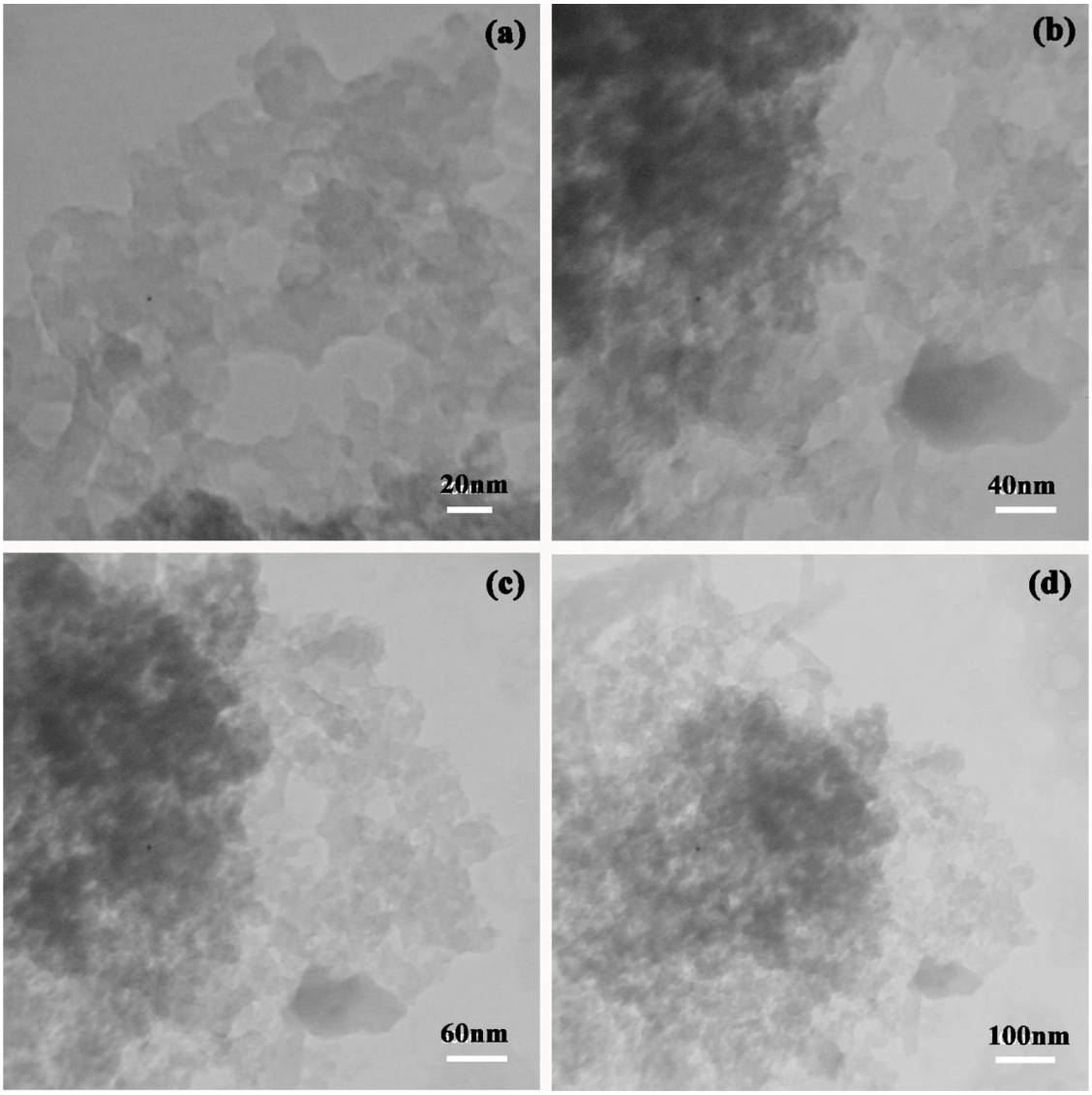

Fig. 6. Morphological investigation of $ErVO_4$ (P1) using TEM images.

and 64.38% efficiency for catalyst loading of 0.03, 0.05 and 0.07 g respectively. By Increasing the catalyst the dye solution environment saturated and led to an irradiation barricade (Sunayana et al., 2010). This pheromone causes to decrease in photocatalytic efficiency by loading 0.07 g catalysts.

The proposed mechanism for the degradation of methylene blue is explained as follows. The methylene blue was excited using the UV light and the electrons from the MB were moved to the conduction band of $ErVO_4$. Those electrons were borrowed by the oxygen species present in the water, which were responsible for the production of reactive oxygen radicals. So, the pair of electron–hole created owing to excitation of $ErVO_4$ under UV illumination which delivers the required circumstances for the creation of reactive oxygen species leads to the organic pollutant removal (Jeyasubramanian et al., 2015). The following equations clarify the several reaction sequences of photocatalytic degradation:

$$MB + hv \rightarrow MB^{*} \quad (1)$$

$$MB^{*} + ErVO_4 \rightarrow ErVO_4^{-1} + MB^{+1} \quad (2)$$

$$ErVO_4^{-1} + O_2 \rightarrow ErVO_4 + O_2^{-1} \quad (3)$$

$$ErVO_4 + hv \rightarrow ErVO_4\ (h^{+} + e^{-}) \quad (4)$$

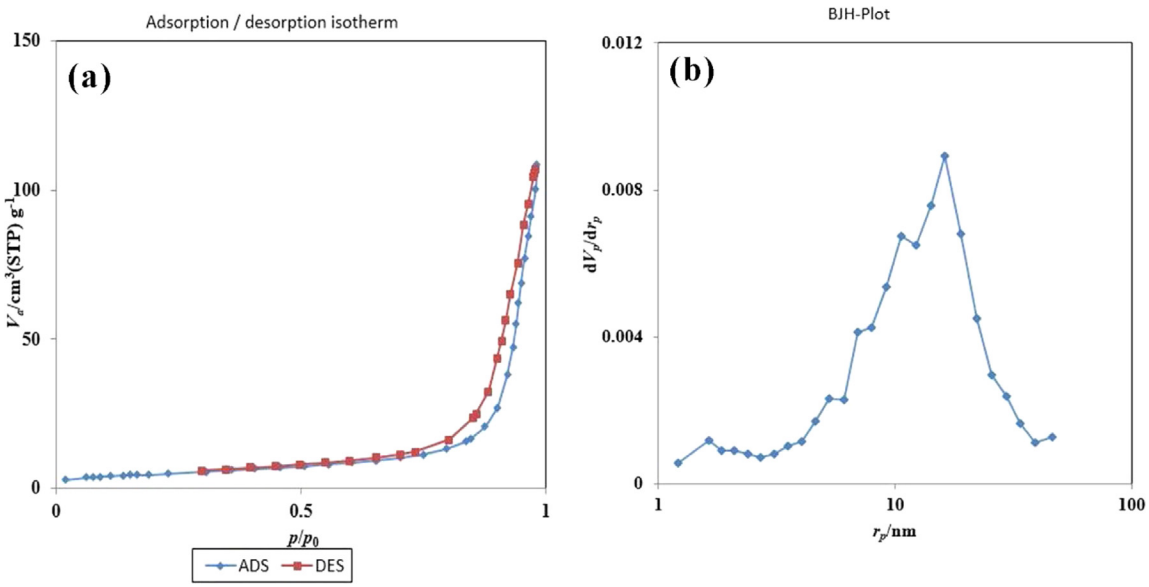

Fig. 7. BET-BJH analysis for sample P1 (Synthesized by citric acid and EG).

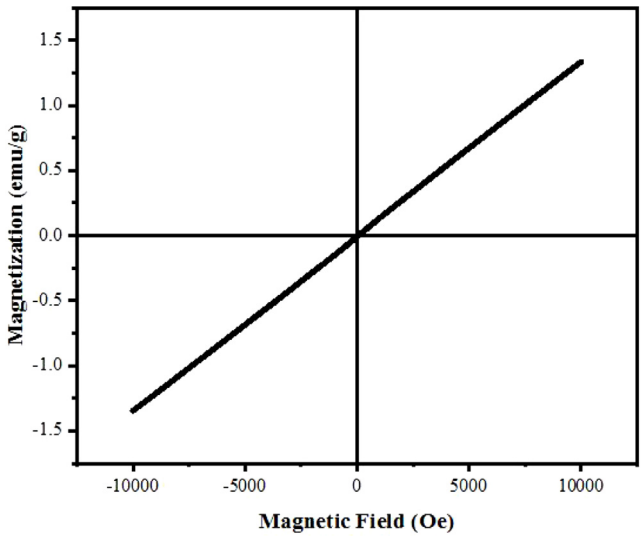

Fig. 8. VSM analysis for sample P1 (Synthesized by citric acid and EG).

$$h^+ + H_2O \rightarrow OH + H^+ \quad (5)$$

$$H^+ + O_2^- \rightarrow HO_2 \quad (6)$$

$$HO_2 \rightarrow H_2O_2 + O_2 \quad (7)$$

$$H_2O_2 + O_2^- \rightarrow OH + OH^- + O_2 \quad (8)$$

$$H_2O_2 + e^- \rightarrow OH + OH^- \quad (9)$$

$$MB + ROS \rightarrow \text{Degraded MB} \quad (10)$$

The removal of dye pollutants can be done with help of active spices such as radicals of hydroxyl, holes and anions of superoxide. The photodegradation direction should be studied in the presence of scavenger species benzoic acid (BA),

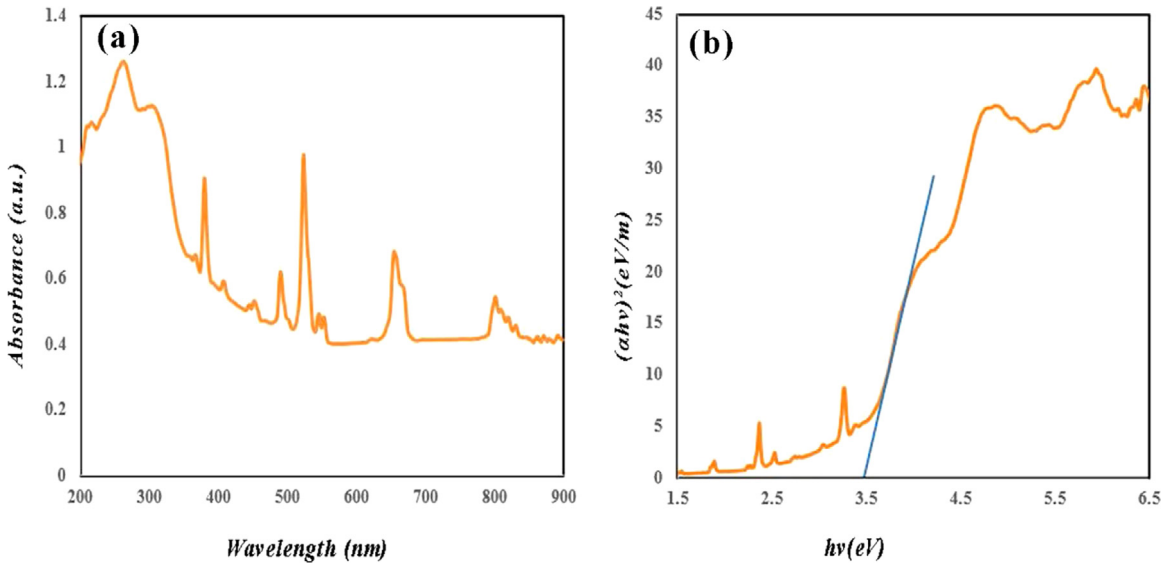

Fig. 9. (a) UV–Vis and (b) band gap determination for sample P1 (Synthesized by citric acid and EG).

Table 2
Comparison of photocatalyst materials with the results of this work in terms of degradation efficiency of colored pollutants.

Photocatalyst	Dye	Time	Light source	Efficiency	Ref.
$CeVO_4$	MB	35 min	UV	63%	Ekthammathat et al. (2013)
$FeVO_4/g\text{-}C_3N_4$	RhB	120 min	350 W Xe lamp	68%	Nong et al. (2015)
$Zn_3(VO_4)_2$	MB	5 h	Visible	37%	Jiang et al. (2017)
$V_2O_3/CNT/TiO_2$	MB	120 min	Visible	70	Chen and Oh (2010)
$YbVO_4$	MO	360 min	Visible	82%	Vadivel et al. (2020)
$Fe_3O_4/CdWO_4$	RhB	80 min	Visible	49%	Sobhani-Nasab et al. (2021)
$ErVO_4$	MB	120 min	UV	77.85%	This Work

Benzoquinone (BQ) and EDTA as scavengers of OH^0, $^0O_2^-$ and h^+ correspondingly (Zhang et al., 1998). The low efficiency in the presence of scavenger species explains the direction mechanism. The percent of dye removal in presence of EDTA, BA and BQ has been discovered in Fig. 10d. The removal efficiency in the presence of BA is lower than EDTA and BQ which considered the role of hydroxyl radical in the photocatalytic removal of methylene blue (Ryu and Choi, 2006).

The comparison photocatalytic test for degradation of MB was performed in the presence of all samples (P1, P2, P3 and P4) which presents in Fig. 10e. the results show better efficiency for sample P1 (77.85%). The removal percentage for samples P2, P3 and P4 are 15.50%, 57.28% and 62.35% correspondingly. According to Fig. 10f, the blank test for degradation of Mo, MB and ER was conducted under UV light in the absence of $ErVO_4$ catalyst. The degradation efficiency is 8.33%, 7.31% and 9.73% for Mo, MB and ER, respectively.

Based on the optimized condition, the 0.05 $ErVO_4$ catalyst in the 10 ppm MB show higher efficiency than other dosage catalysts. Also, the mechanism direction confirms through BA scavenger. Therefore, in order to determine the enough catalyst for finishing the reduction process and high efficiency, the scavenger test was conducted in the presence of different dosage of $ErVO_4$. As shown in Fig. 11, the 0.05 g of $ErVO_4$ in the scavenger test, presents lower response than other dosage which confirms the conducted dosage test (Fig. 10c) in the absence of BA.

The optimized catalyst of $ErVO_4$ was considered in terms of recycling ability after 4 runs which illustrate in Fig. 12. The removal efficiency in 10 ppm of MB with catalyst loading of 0.05 g after 4 runs remains about 69.25% which decreased by 6.9% from the first cycle to the fourth cycle. Correspondingly, the structure of $ErVO_4$ was characterized after recycling in terms of structural stability using X-ray diffraction patterns and Fourier-transform infrared spectroscopy. According to Fig. 13a, the XRD pattern of the recovered catalyst exactly matched the reference pattern of $ErVO_4$ (JCPDS= 86-2349). The obtained chemical bands from FT-IR spectra show no changes against the not reacted catalyst before photocatalyst experiments (Fig. 13b). According to Table 2, several photocatalyst material compared with $ErVO_4$ in terms of degradation efficiency of colored pollutants.

The FT-IR spectrum of MB before degradation is shown in Fig. 14a, and the assignments of spectral peaks are 665, 879, 1135, 1323, 1388, 1592, 1481, 1721 and 2924 cm^{-1} which related to the vibration mode of δ(C–S–C), γ(C–H)

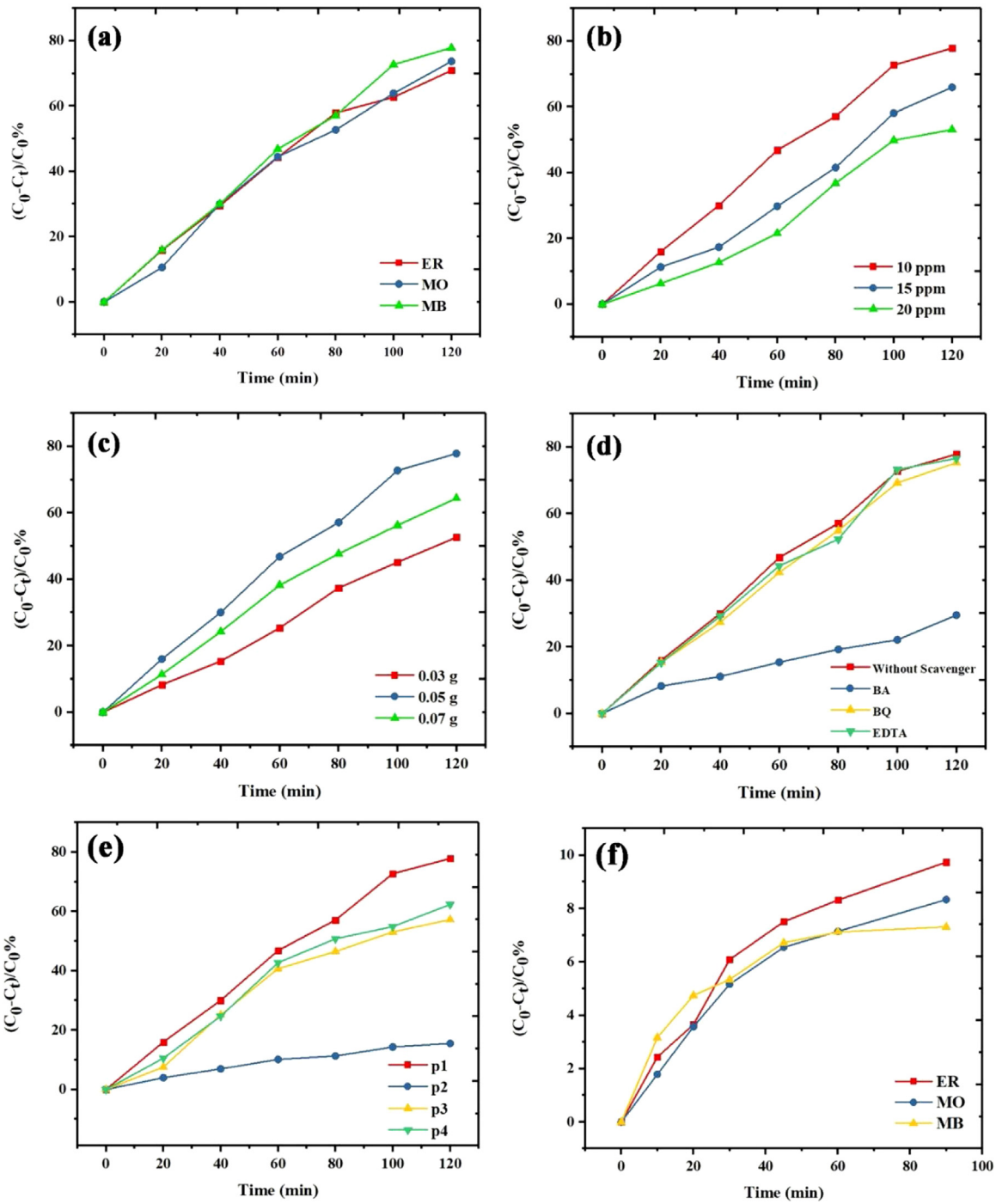

Fig. 10. Study the photocatalytic efficiency of $ErVO_4$ nanoparticles (P1) in different operational conditions (a) effect of colored pollutant model, (b) effect of pollutant concentration, (c) effect of catalyst loading and (d) mechanism study using scavengers, (e) comparison photocatalytic test for sample P1, P2, P3 and P4 and (f) Blank comparison test for different dyes.

aromatic ring, υ(C=S), υ(C–N), γ(C–H) methyl, δ(C=C), υ(C=N) and υ(C–H) methyl, respectively. The FT-IR spectra of the degraded products collected at 120 min is shown in Fig. 14b. In the comparison of Fig. 14a and Fig. 14b, the number of absorption peaks after degradation markedly decreased. The C–S–C skeletal vibration absorption (665 cm^{-1}) related to the chromophoric groups of MB disappeared. The intensity of stretching vibration absorption of C=N (1721 cm^{-1}) and

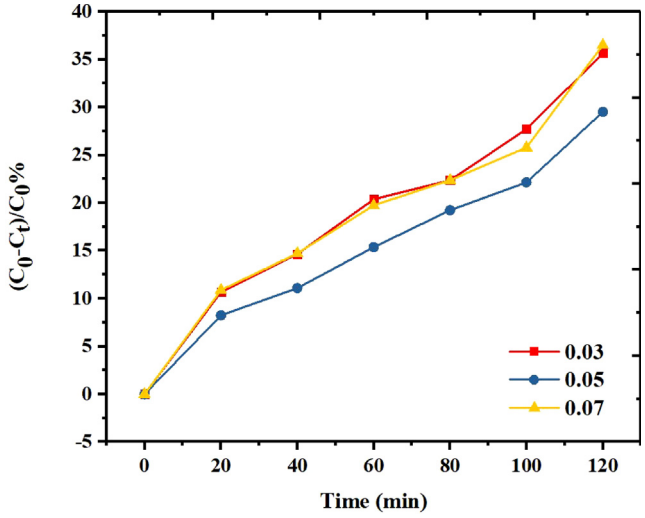

Fig. 11. Scavenger study of BA in the presence of different dosage of catalyst (P1).

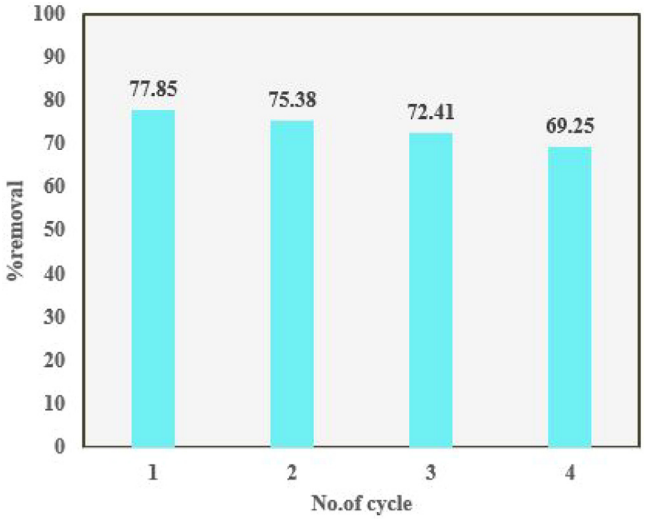

Fig. 12. Recycle ability of $ErVO_4$ nano-photocatalyst after 4 runs.

C=S (1135 cm^{-1}) decreased. This result indicated that the sulfur–nitrogen conjugated system in the MB molecule was destroyed during degradation. The C–N stretching vibration absorption (1323 cm^{-1}) on the aromatic ring disappeared in terms of decreasing the peak intensity; hence, a deamination or denitration reaction occurred during degradation. The C=C skeletal vibration absorption (1592 and 1481 cm^{-1}) and the intensity of C–H deformation vibration absorption (879 cm^{-1}) of the aromatic ring evidently decreased, indicating that the aromatic ring of the MB molecule was severely damaged. This finding indicated that MB was possibly decomposed into small organic molecules, such as hydrocarbons. The absorption peak at 3426 cm^{-1} cans be attributed to the stretching vibration of –OH in the associated alcoholic polymer (Lin et al., 2018).

3.6. EIS and PL analysis

Electrochemical impedance spectroscopy (EIS) was carried out to investigate the migration and transfer processes of photogenerated electrons and holes in the catalyst. The radius of the arc in the EIS spectra reflects the interface layer

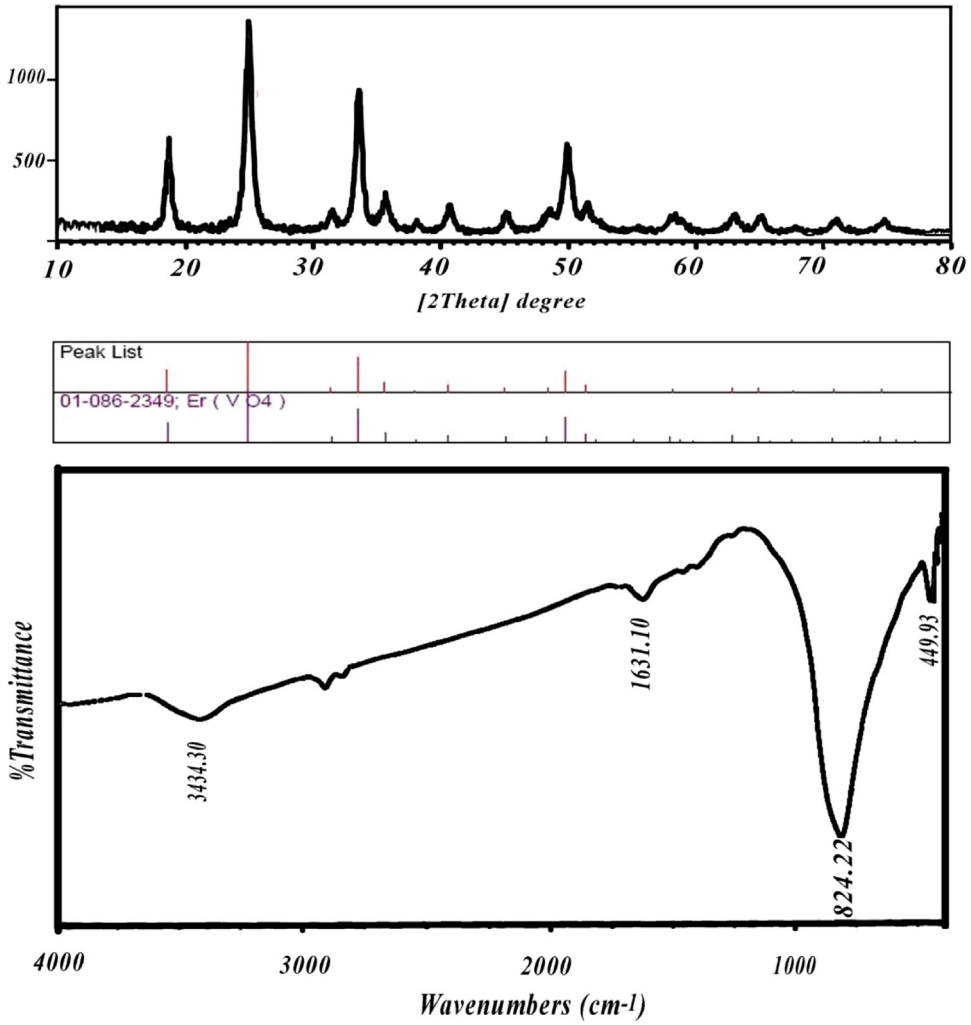

Fig. 13. Structural stability of used $ErVO_4$ nano-photocatalyst after decolorization test.

resistance occurred on the surface of electrode. Generally, the smaller radius of the arc indicates the higher efficiency of charge transfer (Yan et al., 2015). The Nyquist plots of $ErVO_4$ before and after light irradiation is shown in Fig. 15. It can be seen that the arc radius of EIS Nyquist plot of $ErVO_4$ under the light irradiation is smaller than that in the dark, suggesting the dramatically enhanced transfer and separation efficiency of photogenerated carriers and transfer rate of photoexcited electron after light irradiation (Chen et al., 2015; Jing et al., 2016).

Photoluminescence (PL) emission spectra are usually employed to reveal the separation and recombination efficiency of the photogenerated electron–hole pairs in photocatalysts (Di et al., 2015). Fig. 16 presents the PL spectrum of pristine $ErVO_4$ with an excitation wavelength of 399 nm. The PL analysis is consistent with the EIS analysis, further confirms that the $ErVO_4$ is effective photocatalyst candidate for degradation of colored pollutants.

4. Conclusion

Synthesis of tetragonal $ErVO_4$ nanostructures (space group of *I41/amd*) *via* carboxylic-assisted pechini method was successfully conducted to optimize the particle size and properties. The synthesized $ErVO_4$ nanoparticles were subjected to the photocatalytic ability for dye decolorization of Erythrosine (ER), Methyl orange (MO) and Methylene blue (MB) under ultraviolet irradiation. The best catalytic performance of $ErVO_4$ was achieved in the decolorization of MB with an efficiency of about 77.85% with a concentration of 10 ppm and catalyst loading of 0.05 g. The photocatalytic mechanism process was

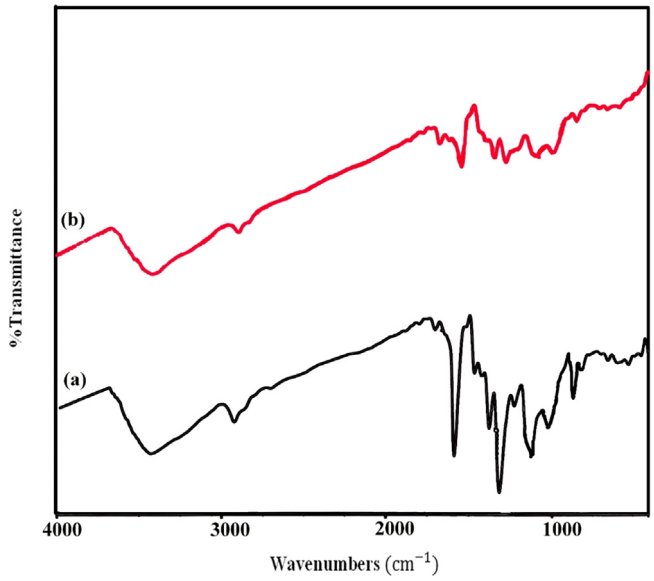

Fig. 14. FT-IR spectra of MB before (a) and after (b) degradation.

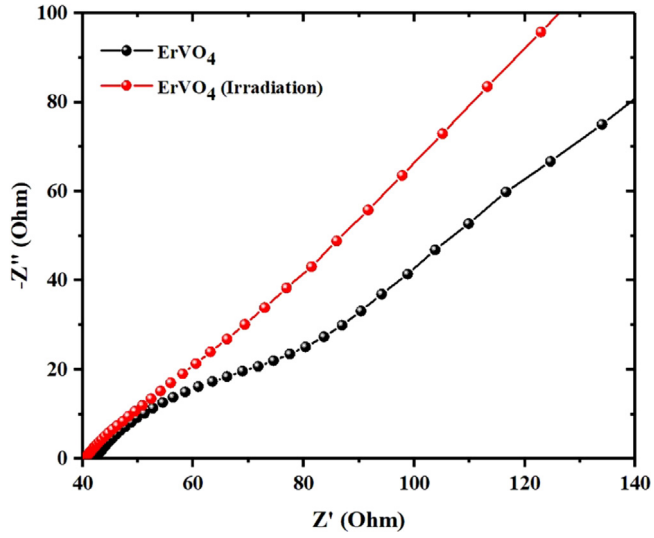

Fig. 15. Electrochemical impedance spectra of $ErVO_4$ photocatalysts before and after irradiation.

studied in the presence of different scavengers which presents the role of hydroxyl radical in the photocatalytic removal of methylene blue. Also, the recycling test for $ErVO_4$ catalyst after 4 runs remains 69.25%. The magnetic behavior for ErVO4 is paramagnetic with saturation magnetization is 1.3341 emu g^{-1} Also, the surface area and average pore size for this sample were calculated at about 16.919 m^2g^{-1} and 39.77 nm for optimized samples with particle sizes in the range of 12-−98 nm.

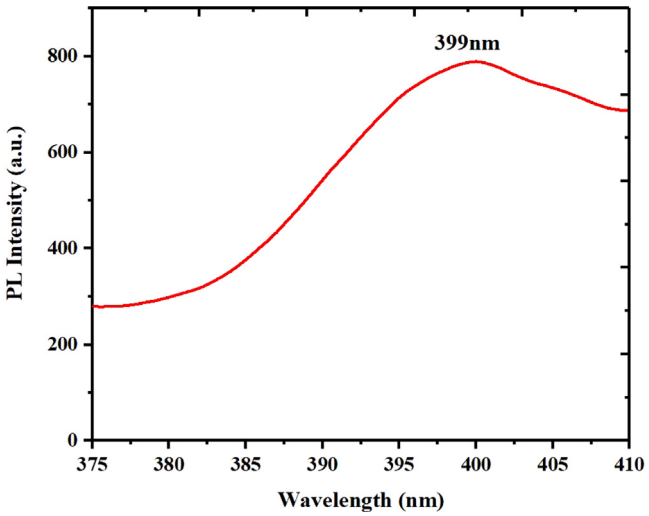

Fig. 16. Photoluminescence spectrum for pristine $ErVO_4$ nanostructures (P1).

CRediT authorship contribution statement

Atefeh Karami: Software, Investigation, Methodology, Formal analysis. **Rozita Monsef:** Formal analysis, Data curation, Investigation, Software, Writing – review & editing. **Mustafa Ridha Shihan:** Software, Writing – review & editing. **Laith Yassen Qassem:** Software, Visualization. **Mayadah W. Falah:** Software. **Masoud Salavati-Niasari:** Formal analysis, Methodology, Writing – review & editing, Writing – original draft, Conceptualization, Supervision, Project administration, Investigation, Data curation, Validation, Resources, Visualization, Funding acquisition.

Declaration of competing interest

The authors declare that they have no known competing financial interests or personal relationships that could have appeared to influence the work reported in this paper.

Data availability

The authors do not have permission to share data.

Acknowledgments

Authors are thankful to the council of the Iran National Science Foundation; INSF (97017837) and University of Kashan, Iran for supporting this work by Grant No (159271/AK2).

References

Abdulsahib, W.K., Sahib, H.H., Mahdi, M.A., Jasim, L.S., 2021. Adsorption study of cephalexin monohydrate drug in solution on poly (vinyl pyrrolidone-acryl amide) hydrogel surface. Int. J. Drug Deliv. Technol. 11 (4), 1169–1172. http://dx.doi.org/10.25258/ijddt.11.4.9.

Abedini, A., 2017. Nanocrystalline ErVO4: Synthesis, characterization, optical and photocatalytic properties. J. Mater. Sci.: Mater. Electron. 28 (12), 8446–8451.

Ahmad, P.T., Jaleh, B., Nasrollahzadeh, M., Issaabadi, Z., 2019. Efficient reduction of waste water pollution using GO/γ MnO2/Pd nanocomposite as a highly stable and recoverable catalyst. Sep. Purif. Technol. 225, 33–40.

Aljeboree, A.M., Alrazzak, N.A., Alqaraguly, M.B., Mahdi, M.A., Jasim, L.S., Alkaim, A.F., 2020. Adsorption of pollutants by using low-cost (environment-friendly): Equilibrium, kinetics and thermodynamic studies: A review. Syst. Rev. Pharmacy 11 (12), 1988–1997. http://dx.doi.org/10.31838/srp.2020.12.303.

Aljeboree, A.M., Mohammed, R.A., Mahdi, M.A., Jasim, L.S., Alkaim, A.F., 2021. Synthesis, characterization of P(Ch/Aa-Co-Am) and adsorptive removal of Pb(Ii) ions from aqueous solution: Thermodynamic study. NeuroQuantology 19 (7), 137–143. http://dx.doi.org/10.14704/nq.2021.19.7.NQ21096.

AlNadhari, S., Al-Enazi, N.M., Alshehrei, F., Ameen, F., 2021. A review on biogenic synthesis of metal nanoparticles using marine algae and its applications. Environ. Res. 194, 110672.

Alshamusi, Q.K.M., Alzayd, A.A.M., Mahdi, M.A., Jasim, L.S., Aljeboree, A.M., 2021. Adsorption OF CRYSTAL violate (CV) DYE IN AQUEOUS SOLUTIONS BY USING P(PVP-CO-AAM)/GO COMPOSITE AS (ECO-HEALTHY ADSORBATE SURFACE): Characterization AND thermodynamics STUDIES. Biochem. Cell. Arch. 21, 2423–2431.

Ameen, F., Al-Homaidan, A.A., Al-Sabri, A., Almansob, A., AlNAdhari, S., 2021. Anti-oxidant, anti-fungal and cytotoxic effects of silver nanoparticles synthesized using marine fungus cladosporium halotolerans. Appl. Nanosci. 1–9.

Ameen, F., Srinivasan, P., Selvankumar, T., Kamala-Kannan, S., Al Nadhari, S., Almansob, A., Dawoud, T., Govarthanan, M., 2019. Phytosynthesis of silver nanoparticles using Mangifera indica flower extract as bioreductant and their broad-spectrum antibacterial activity. Bioorg. Chem. 88, 102970.
Chen, M.-L., Oh, W.-C., 2010. The improved photocatalytic properties of methylene blue for V₂O₃/CNT/TiO₂ composite under visible light. Int. J. Photoenergy 2010, 264831.
Chen, D., Wang, K., Hong, W., Zong, R., Yao, W., Zhu, Y., 2015. Visible light photoactivity enhancement via CuTCPP hybridized g-C3N4 nanocomposite. Appl. Catal. B 166, 366–373.
de Luna, M.D.G., Flores, E.D., Genuino, D.A.D., Futalan, C.M., Wan, M.-W., 2013. Adsorption of eriochrome black T (EBT) dye using activated carbon prepared from waste rice hulls—Optimization, isotherm and kinetic studies. J. Taiwan Inst. Chem. Eng. 44 (4), 646–653.
Di, J., Xia, J., Ge, Y., Li, H., Ji, H., Xu, H., Zhang, Q., Li, H., Li, M., 2015. Novel visible-light-driven CQDs/Bi2WO6 hybrid materials with enhanced photocatalytic activity toward organic pollutants degradation and mechanism insight. Appl. Catal. B 168, 51–61.
Ekthammathat, N., Thongtem, T., Phuruangrat, A., Thongtem, S., 2013. Synthesis and characterization of CeVO4 by microwave radiation method and its photocatalytic activity. J. Nanomater. 2013, 5.
Fadillah, G., Hidayat, R., Saleh, T.A., 2022. Hydrothermal assisted synthesis of titanium dioxide nanoparticles modified graphene with enhanced photocatalytic performance. J. Ind. Eng. Chem..
Fernandez-Garcia, M., Martinez-Arias, A., Hanson, J., Rodriguez, J., 2004. Nanostructured oxides in chemistry: Characterization and properties. Chem. Rev. 104 (9), 4063–4104.
Ganduh, S.H., Aljeboree, A.M., Mahdi, M.A., Jasim, L.S., 2021a. Spectrophotometric determination of metoclopramide-HCL in the standard raw and it compared with pharmaceuticals. J. Pharm. Negat. Results 12 (2), 44–48. http://dx.doi.org/10.47750/pnr.2021.12.02.008.
Ganduh, S.H., Kmal, R.Q., Mahdi, M.A., Aljeboree, A.M., Jasim, L.S., 2021b. Selective spectrophotometric determination of 4-amino antipyrine antibiotics in pure forms and their pharmaceutical formulations. Int. J. Drug Deliv. Technol. 11 (2), 371–375. http://dx.doi.org/10.25258/ijddt.11.2.23.
Ghiyasiyan-Arani, M., Masjedi-Arani, M., 2016. Size controllable synthesis of cobalt vanadate nanostructures with enhanced photocatalytic activity for the degradation of organic dyes. J. Mol. Catal. A: Chem. 425, 31–42.
Ghiyasiyan-Arani, M., Masjedi-Arani, M., Salavati-Niasari, M., 2016a. Facile synthesis, characterization and optical properties of copper vanadate nanostructures for enhanced photocatalytic activity. J. Mater. Sci.: Mater. Electron. 27 (5), 4871–4878.
Ghiyasiyan-Arani, M., Masjedi-Arani, M., Salavati-Niasari, M., 2016b. Novel Schiff base ligand-assisted in-situ synthesis of Cu3V2O8 nanoparticles via a simple precipitation approach. J. Molecular Liquids 216, 59–66.
Grabowska, E., 2016. Selected perovskite oxides: Characterization, preparation and photocatalytic properties—A review. Appl. Catal. B: Environ. 186, 97–126.
Hunge, Y.M., Uchida, A., Tominaga, Y., Fujii, Y., Yadav, A.A., Kang, S.-W., Suzuki, N., Shitanda, I., Kondo, T., Itagaki, M., 2021. Visible light-assisted photocatalysis using spherical-shaped bivo4 photocatalyst. Catalysts 11 (4), 460.
Jaleh, B., Karami, S., Sajjadi, M., Feizi Mohazzab, B., Azizian, S., Nasrollahzadeh, M., Varma, R.S., 2020. Laser-assisted preparation of pd nanoparticles on carbon cloth for the degradation of environmental pollutants in aqueous medium. Chemosphere 246, 125755.
Jasim, L.S., Aljeboree, A.M., Sahib, I.J., Mahdi, M.A., Abdulrazzak, F.H., Alkaim, A.F., 2022. Effective adsorptive removal of riboflavin (RF) over activated carbon. AIP Conf. Proc. 2386, 030030. http://dx.doi.org/10.1063/5.0066996.
Jeyasubramanian, K., Hikku, G.S., Sharma, R.K., 2015. Photo-catalytic degradation of methyl violet dye using zinc oxide nano particles prepared by a novel precipitation method and its anti-bacterial activities. J. Water Process Eng. 8, 35–44.
Ji, Y., Hu, J., Biskupek, J., Kaiser, U., Song, Y.F., Streb, C., 2017. Polyoxometalate-based bottom-up fabrication of graphene quantum dot/manganese vanadate composites as lithium ion battery anodes. Chem. Eur. J. 23 (65), 16637–16643.
Jiang, Y., Liu, P., Tian, S., Liu, Y., Peng, Z., Li, F., Ni, L., Liu, Z., 2017. Sustainable visible-light-driven Z-scheme porous Zn3(VO4)2/g-C3N4 heterostructure toward highly photoredox pollutant and mechanism insight. J. Taiwan Inst. Chem. Eng. 78, 517–529.
Jing, L., Xu, Y., Huang, S., Xie, M., He, M., Xu, H., Li, H., Zhang, Q., 2016. Novel magnetic CoFe2O4/Ag/Ag3VO4 composites: Highly efficient visible light photocatalytic and antibacterial activity. Appl. Catal. B 199, 11–22.
Kim, D.H., Kang, Y.-M., Ur, S.-C., You, J.-H., Yoo, S.-I., 2018. Structure and magnetic properties of La0. 7Sr0. 3MnO3 (1- x)–SrFe12O19 (x) composites. J. Magn. Magn. Mater. 449, 567–570.
Leofanti, G., Padovan, M., Tozzola, G., Venturelli, B., 1998. Surface area and pore texture of catalysts. Catal. Today 41 (1–3), 207–219.
Li, L., Niu, C.-G., Guo, H., Wang, J., Ruan, M., Zhang, L., Liang, C., Liu, H.-Y., Yang, Y.-Y., 2020. Efficient degradation of levofloxacin with magnetically separable ZnFe2O4/NCDs/Ag2CO3 Z-scheme heterojunction photocatalyst: Vis-NIR light response ability and mechanism insight. Chem. Eng. J. 383, 123192.
Lin, J., Luo, Z., Liu, J., Li, P., 2018. Photocatalytic degradation of methylene blue in aqueous solution by using ZnO-SnO2 nanocomposites. Mater. Sci. Semicond. Process. 87, 24–31.
Liu, H.-Y., Niu, C.-G., Guo, H., Huang, D.-W., Liang, C., Yang, Y.-Y., Tang, N., Zhang, X.-G., 2022. Integrating the Z-scheme heterojunction and hot electrons injection into a plasmonic-based Zn2In2S5/W18O49 composite induced improved molecular oxygen activation for photocatalytic degradation and antibacterial performance. J. Colloid Interface Sci. 610, 953–969.
Mahdi, M.A., Aljeboree, A.M., Jasim, L.S., Alkaim, A.F., 2021. Synthesis, characterization and adsorption studies of a graphene oxide/polyacrylic acid nanocomposite hydrogel. NeuroQuantology 19 (9), 46–54. http://dx.doi.org/10.14704/nq.2021.19.9.NQ21136.
Mahdi, M.A., Jasim, L.S., Mohamed, M.H., 2020. Synthesis and anticancer activity evaluation of novel ligand 2- [2 - (5-chloro carboxy phenyl) azo] 1-methyl imidazole (1-Mecpai) with some metal complexes. Syst. Rev. Pharmacy 11 (12), 1979–1987. http://dx.doi.org/10.31838/srp.2020.12.302.
Mahdi, M.A., Jasim, L.S., Ranjeh, M., Masjedi-Arani, M., Salavati-Niasari, M., 2022. Improved pechini sol–gel fabrication of Li2B4O7/NiO/Ni3(BO3)2 nanocomposites to advanced photocatalytic performance. Arab. J. Chem. 15 (5), 103768. http://dx.doi.org/10.1016/j.arabjc.2022.103768.
Mamonova, D., Kolesnikov, I., Manshina, A., Mikhailov, M., Smirnov, V., 2017. Modified Pechini method for the synthesis of weakly-agglomerated nanocrystalline yttrium aluminum garnet (YAG) powders. Mater. Chem. Phys. 189, 245–251.
Moghadam, N.C.Z., Jasim, S.A., Ameen, F., Alotaibi, D.H., Nobre, M.A.L., Sellami, H., Khatami, M., 2022. Nickel oxide nanoparticles synthesis using plant extract and evaluation of their antibacterial effects on Streptococcus mutans. Bioprocess Biosyst. Eng. 45 (7), 1201–1210.
Musadiq Anis, S., Habibullah Hashemi, S., Nasri, A., Sajjadi, M., Eslamipanah, M., Jaleh, B., 2022. Decorated ZrO2 by Au nanoparticles as a potential nanocatalyst for the reduction of organic dyes in water. Inorg. Chem. Commun. 141, 109489.
Mythili, R., Selvankumar, T., Srinivasan, P., Sengottaiyan, A., Sabastinraj, J., Ameen, F., Al-Sabri, A., Kamala-Kannan, S., Govarthanan, M., Kim, H., 2018. Biogenic synthesis, characterization and antibacterial activity of gold nanoparticles synthesised from vegetable waste. J. Mol. Liquids 262, 318–321.
Nasri, A., Jaleh, B., Nezafat, Z., Nasrollahzadeh, M., Azizian, S., Jang, H.W., Shokouhimehr, M., 2021. Fabrication of g-C3N4/Au nanocomposite using laser ablation and its application as an effective catalyst in the reduction of organic pollutants in water. Ceram. Int. 47 (3), 3565–3572.
Nong, Q., Cui, M., Lin, H., Zhao, L., He, Y., 2015. Fabrication, characterization and photocatalytic activity of G-C3N4 coupled with FeVO4 nanorods. RSC Adv. 5 (35), 27933–27939.
Obregón, S., Vázquez, A., Hernández-Uresti, D., 2018. Nanocrystalline ErVO4 as a novel photocatalyst for degradation of organic compounds and solar fuels production. J. Mater. Sci., Mater. Electron. 29 (5), 3967–3972.

Ryu, J., Choi, W., 2006. Photocatalytic oxidation of arsenite on TiO2: Understanding the controversial oxidation mechanism involving superoxides and the effect of alternative electron acceptors. Environ. Sci. Technol. 40 (22), 7034–7039.
Saravanan, M., Gopinath, V., Chaurasia, M.K., Syed, A., Ameen, F., Purushothaman, N., 2018. Green synthesis of anisotropic zinc oxide nanoparticles with antibacterial and cytofriendly properties. Microb. Pathog. 115, 57–63.
Sobhani-Nasab, A., Hoseinpour, S.M., Rahimi-Nasrabadi, M., Pourmasoud, S., Eghbali-Arani, M., Ahmadi, F., 2021. Synthesis of Fe3O4/CdWO4/carbon dots heterostructure with excellent visible light photocatalytic stability and activity for degradation of 4-nitrophenol and organic pollutant. J. Mater. Sci., Mater. Electron. 32 (22), 26998–27013.
Souza, D.R., Neves, J.V.S., França, Y.K., Malheiro, W.C., 2021. TiO2 synthesis by the Pechini's method and application for diclofenac photodegradation. Photochem. Photobiol. 97 (1), 32–39.
Sunayana, S., Nitin, C., Chaturvedi, R., Sharma, M., 2010. Photocatalytic degradation of eriochrome black T using ammonium phosphomolybdate semiconductor. Int. J. Chem. Sci. 8 (3), 1580–1590.
Vadivel, S., Paul, B., Kumaravel, M., Hariganesh, S., Rajendran, S., Prasanga Gayanath Mantilaka, M.M.M.G., Mamba, G., Puviarasu, P., 2020. Facile synthesis of YbVO4, and YVO4 nanostructures through MOF route for photocatalytic applications. Inorg. Chem. Commun. 115, 107855.
Wang, H., Zhang, L., Chen, Z., Hu, J., Li, S., Wang, Z., Liu, J., Wang, X., 2014. Semiconductor heterojunction photocatalysts: Design, construction, and photocatalytic performances. Chem. Soc. Rev. 43 (15), 5234–5244.
Yan, T., Sun, M., Liu, H., Wu, T., Liu, X., Yan, Q., Xu, W., Du, B., 2015. Fabrication of hierarchical BiOI/Bi2MoO6 heterojunction for degradation of bisphenol A and dye under visible light irradiation. J. Alloys Compd. 634, 223–231.
Yang, Y.-Y., Zhang, X.-G., Niu, C.-G., Feng, H.-P., Qin, P.-Z., Guo, H., Liang, C., Zhang, L., Liu, H.-Y., Li, L., 2020. Dual-channel charges transfer strategy with synergistic effect of Z-scheme heterojunction and LSPR effect for enhanced quasi-full-spectrum photocatalytic bacterial inactivation: New insight into interfacial charge transfer and molecular oxygen activation. Appl. Catal. B 264, 118465.
Zhang, W., Au, C., Wan, H., 1998. Active site of praseodymium orthovanadate catalyst in oxidative dehydrogenation of propane. Chin. Sci. Bull. 43 (3), 217–220.
Zonarsaghar, A., Mousavi-Kamazani, M., Zinatloo-Ajabshir, S., 2022. Sonochemical synthesis of CeVO4 nanoparticles for electrochemical hydrogen storage. Int. J. Hydrogen Energy 47 (8), 5403–5417.